

# Impedimetric Microfluidic Sensor-in-a-Tube for Label-Free Immune Cell Analysis

Aleksandr I. Egunov,\* Zehua Dou, Dmitriy D. Karnaushenko, Franziska Hebenstreit, Nicole Kretschmann, Katja Akgün, Tjalf Ziemssen, Daniil Karnaushenko,\* Mariana Medina-Sánchez,\* and Oliver G. Schmidt\*

Analytical platforms based on impedance spectroscopy are promising for non-invasive and label-free analysis of single cells as well as of their extracellular matrix, being essential to understand cell function in the presence of certain diseases. Here, an innovative rolled-up impedimetric microfluidic sensor, called sensor-in-a-tube, is introduced for the simultaneous analysis of single human monocytes CD14+ and their extracellular medium upon liposaccharides (LPS)-mediated activation. In particular, rolled-up platinum microelectrodes are integrated within for the static and dynamic (in-flow) detection of cells and their surrounding medium (containing expressed cytokines) over an excitation frequency range from  $10^2$  to  $5 \times 10^6$  Hz. The correspondence between cell activation stages and the electrical properties of the cell surrounding medium have been detected by electrical impedance spectroscopy in dynamic mode without employing electrode surface functionalization or labeling. The designed sensor-in-a-tube platform is shown as a sensitive and reliable tool for precise single cell analysis toward immune-deficient diseases diagnosis.

channels for proper sample handling and processing. These systems are envisioned for diverse medical point-of-care devices as well as laboratory scale medical appliances where an early and personalized disease diagnosis is required for effective therapy.<sup>[1]</sup>

Important targets for these systems are immune-mediated diseases which have become more and more common in the last decades, especially in industrialized countries, affecting millions of people worldwide every year.<sup>[2–4]</sup> Multiple sclerosis, type I diabetes, arthritis, and inflammatory bowel diseases are some examples that require an early and personalized diagnosis.<sup>[1]</sup> However, performing an accurate diagnosis is very challenging due to the heterogeneities among patient samples and different disease progression states. For that reason, novel diagnostic platforms that resolve single cells and their surrounding media with high sensi-

tivity and throughput are required. Nowadays, several methods exist for high-throughput cell analysis such as flow<sup>[5–8]</sup> and laser scanning cytometry,<sup>[9]</sup> RAMAN spectroscopy,<sup>[10–12]</sup> and automatic microscopy.<sup>[13,14]</sup> However, the need of bulky and expensive optics in these techniques hampers their broad application potential into personal care. Previous works related to in-flow detection of single cells,<sup>[15]</sup> and in particular of immune cells have been already reported with some of those techniques,<sup>[16]</sup>

## 1. Introduction

Microscale analytical platforms relying on electrochemical impedance spectroscopy (EIS) have received much attention in recent years due to their sensitivity, high throughput, small scale, and low fabrication costs. Moreover, EIS sensors have been already shown to be compact, fabricated in large scale, containing not only sensing electrodes but also microfluidic

Dr. A. I. Egunov, Z. Dou, Dr. D. D. Karnaushenko, F. Hebenstreit, Dr. D. Karnaushenko, Dr. M. Medina-Sánchez, Prof. O. G. Schmidt  
Institute for Integrative Nanosciences  
Leibniz IFW Dresden  
Helmholtzstraße 20, 01069 Dresden, Germany  
E-mail: aleksandr.egunov@gmail.com; d.karnaushenko@ifw-dresden.de; m.medina.sanchez@ifw-dresden.de; o.schmidt@ifw-dresden.de

 The ORCID identification number(s) for the author(s) of this article can be found under <https://doi.org/10.1002/smll.202002549>.

© 2021 The Authors. Small published by Wiley-VCH GmbH. This is an open access article under the terms of the Creative Commons Attribution-NonCommercial-NoDerivs License, which permits use and distribution in any medium, provided the original work is properly cited, the use is non-commercial and no modifications or adaptations are made.

N. Kretschmann, Dr. K. Akgün, Prof. T. Ziemssen  
Center of Clinical Neuroscience  
Multiple Sklerose Zentrum Dresden  
University Hospital Carl Gustav Carus at  
Dresden University of Technology  
Fetscherstr. 74, 01307 Dresden, Germany  
Prof. O. G. Schmidt  
Material Systems for Nanoelectronics  
Chemnitz University of Technology  
Str. der Nationen 62, 09111 Chemnitz, Germany  
Prof. O. G. Schmidt  
Nanophysics  
Dresden University of Technology  
Haeckelstraße 3, 01069 Dresden, Germany

DOI: 10.1002/smll.202002549

as well as the detection of expressed cell proteins (cytokines).<sup>[17]</sup> Among these proteins, cytokines TNF- $\alpha$ ,<sup>[18]</sup> IL-1 $\beta$ , IL-2,<sup>[19]</sup> IL-6, IL-8, IL-10, and IL-12,<sup>[20]</sup> expressed by, that is, lipopolysaccharide (LPS)-activated monocytes CD14+,<sup>[21–23]</sup> are the most prominent markers which provide insights about different stages of immune cell activation, being of crucial importance in immune diseases diagnosis. Some of these cytokines have been individually detected using EIS sensors, functionalized with specific antibodies.<sup>[19,24,25]</sup> However, label and functionalization-free analysis of immune cells as well as a variety of inflammatory cytokines at high throughput have not been reported up to now. In most cases, samples need to be labeled prior to analysis, requiring additional functionalization protocols and consumption of precious samples and reagents. In this respect, EIS microfluidic sensors offer functionalization and label-free detection of small volume samples with high accuracy and throughput.<sup>[26]</sup> Therefore, here we present an ultra-compact and sensitive impedimetric microtubular sensor prepared at wafer scale with shapeable materials<sup>[27]</sup> and self-assembly methods<sup>[28]</sup> allowing static and dynamic (in-flow) analysis of cells in a label- and functionalization-free regime. We prepare Pt electrodes onto a stack of patterned polymeric layers, using conventional planar photolithography techniques, followed by their self-assembly into rolled-up tubular structures and integration into a microfluidic channel. All employed materials are biocompatible with no reported cytotoxicity.<sup>[29–32]</sup> We characterize the sensors and analyze different ionic solutions, single polymeric spheres, and living immune cells in both static and dynamic modes,

as well as the culturing medium containing the cell-secreted cytokines after LPS activation. Combined with high mechanical stability, non-toxicity and optical transparency, the EIS sensor-in-a-tube is capable to analyze: single cells or clusters from a whole cell population as well as the overall influence of secreted cytokines and metabolism products on the electrical properties of cell surrounding medium. We also propose an equivalent circuit which models the performance of the proposed rolled-up sensor when detecting electrolytes and single cells, considering different geometric parameters.

## 2. Results and Discussions

### 2.1. Sensor-in-a-Tube Fabrication

Our EIS chips (Figure 1a–c) consist of multiple 3D platinum microelectrodes, patterned onto a polymeric layer which is then rolled-up forming a microtube, and embedded into a polydimethylsiloxane (PDMS) microfluidic channel for further sample handling and detection. Initially, the planar stack is processed using conventional parallel photolithography and thin-film deposition methods, resulting in three polymer layers: a sacrificial layer (SL), a hydrogel swelling layer (HG), a reinforcing polyimide support layer (PI), and platinum electrodes (Pt). This stack is reshaped into “swiss-roll” microtubes by soaking the substrates into the sacrificial layer etching solution (details are in the Experimental Section and displayed in

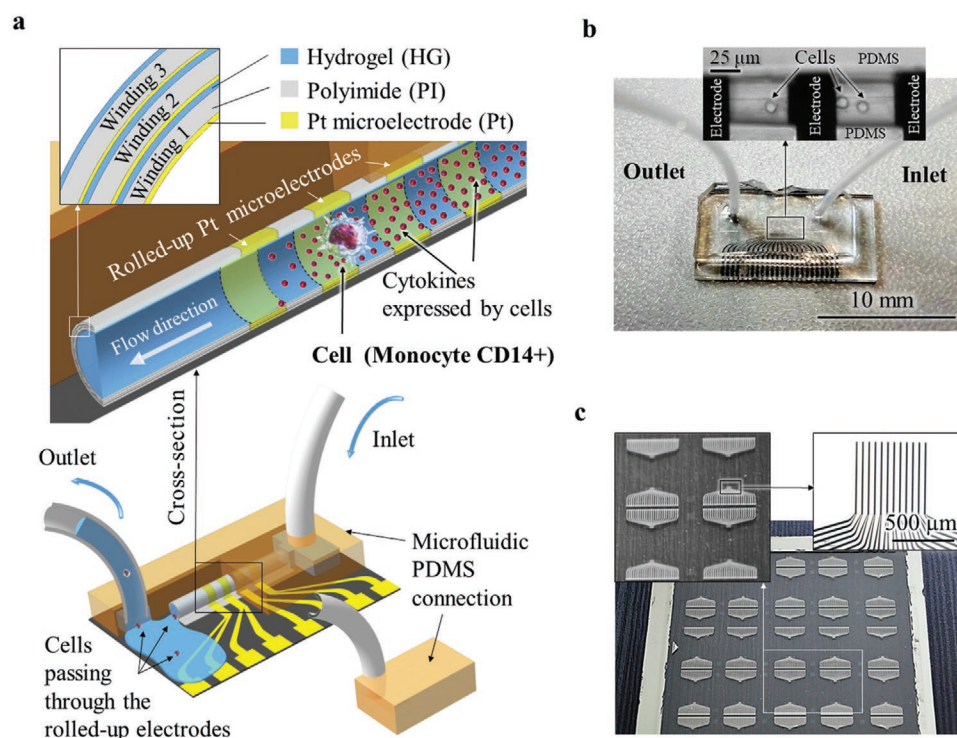


**Figure 1.** Concept of sensor-in-a-tube for label-free detection of single cells and of its extracellular medium analysis. a) Schematic representation of the sensor-in-a-tube integrated into a microfluidic channel. The sensor consists of a self-assembled polymeric tube with integrated Pt microelectrodes. For analysis, the cells are introduced inside the sensor via microfluidic pumping. During the flow, the signal from single cells as well as of their surrounding media is recorded and analyzed by EIS. Additional optical monitoring is possible due to the transparent gaps between the electrode pads. b) Photo of the assembled device with the corresponding external tubing connection, and c) wafer-scale production process of rolled-up microelectrodes onto a 10 cm<sup>2</sup> glass substrate.

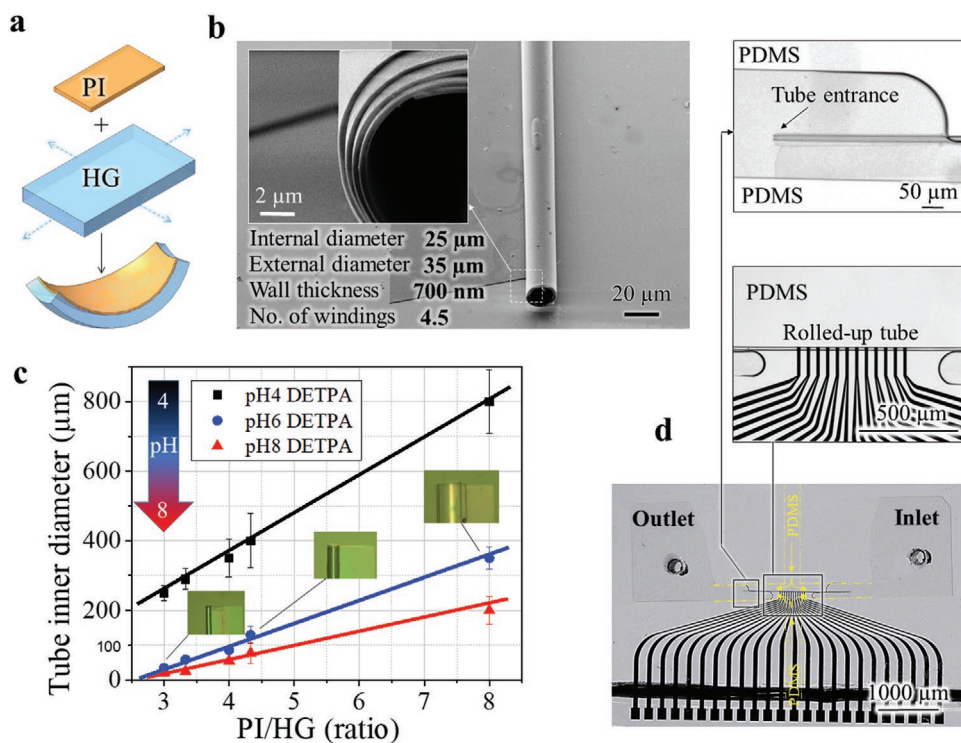


**Figure 2.** Rolled-up microtube fabrication. a) Schematic of intrinsic strain formation in the polymeric stack during swelling in aqueous media. b) SEM images of the microtube with four windings and the diameter fitted to the living cell size ( $\approx 20 \mu\text{m}$ ). c) Influence of polymeric stack thickness ratio as well as of the rolling solution pH on the inner tube diameter. Increasing of PI/HG ratio leads to larger tube diameters. Adversely, increasing the pH of the rolling medium leads to an increase of the HG swelling force that induces a tighter rolling and a smaller tube diameter. d) Encapsulation of the microtube with rolled up electrodes into a PDMS microfluidic channel.

Figure S1, Supporting Information), which simultaneously swells the HG layer.

The HG layer reinforced by the PI layer<sup>[33]</sup> induces differential strain that curls the stack upwards (Figure 2a) resulting in microtubular channels (Figure 2b) with electrodes on their inner surfaces. The HG layer, however, is prone to release the strain once dried (a necessary step prior to integration into the microfluidic chip), resulting in self-disassembly of the prepared structures, and therefore the self-assembled structures must be stabilized. To do so, the wet tubular structures are soaked into a camphor-saturated solution containing a small amount of water and acetone. When acetone evaporates, camphor crystallizes effectively, fixing the geometry of the microtubular architecture. Solid camphor evaporates much slower than water at normal conditions and protects the tube from unrolling during the drying process (Figure 2b and Video S1, Supporting Information). Completely evaporated, camphor leaves no contaminations or residuals within the tubular structures (details are in Experimental Section).

We fabricated 10 mm long mechanically stable and geometrically straight microtubular structures, whose final self-assembled diameter was tuned between 20 and 120  $\mu\text{m}$  by adjusting the thickness of the HG and PI layers (Figure 2c). We chose an optimal thickness ratio of HG/PI = 1/3 to achieve good mechanical stability (Figure S2, Supporting Information) and an appropriate tube diameter which fits to the immune cell size ( $\approx 20 \mu\text{m}$ ). The Pt electrodes were deposited via sputtering onto the PI surface and then patterned before self-assembly (further details are in Note S1, Supporting Information). Width

and gap distance between electrodes along the microtube axis were designed to be 20 and 50  $\mu\text{m}$  respectively. The transparent sections in between the electrodes were used for cell visualization through optical microscopy (Figure 1b inset).

Self-assembled and stabilized structures were then integrated within PDMS molded channels (Figure 1b) by using a conventional mask aligner system (details are described in Experimental Section and displayed in Figure S1b, Supporting Information) and standard oxygen plasma activated bonding, which permits an average fluid pressure of  $\approx 250 \text{ kPa}$ .<sup>[34–36]</sup> The mold was designed with additional lateral microchannels, which served as dispenser of liquid PDMS that was rapidly cross-linked to embed the tubular electrodes within the microchannel, ensuring the pass of the fluid only through the lumen of the tubular electrode (Figure 2d). Finally, the finished chips were connected to a syringe pump via PTFE tubes ( $\varnothing_{\text{int.}} 0.3 \text{ mm}$ ,  $\varnothing_{\text{ext.}} 0.6 \text{ mm}$ ) to introduce the analytes for further experiments.

## 2.2. Calibration and Characterization

Electrodes integrated into the PDMS chip were characterized in pairs along the tube axis using four terminal sensing as shown in Figure 3a. The signal between neighboring electrodes with constant gap distance showed no difference in the impedance Bode plots of PBS 1X solution (Figure S3a, Supporting Information) allowing parallel-electrode measurements with high reproducibility (Figure S3b, Supporting Information). To

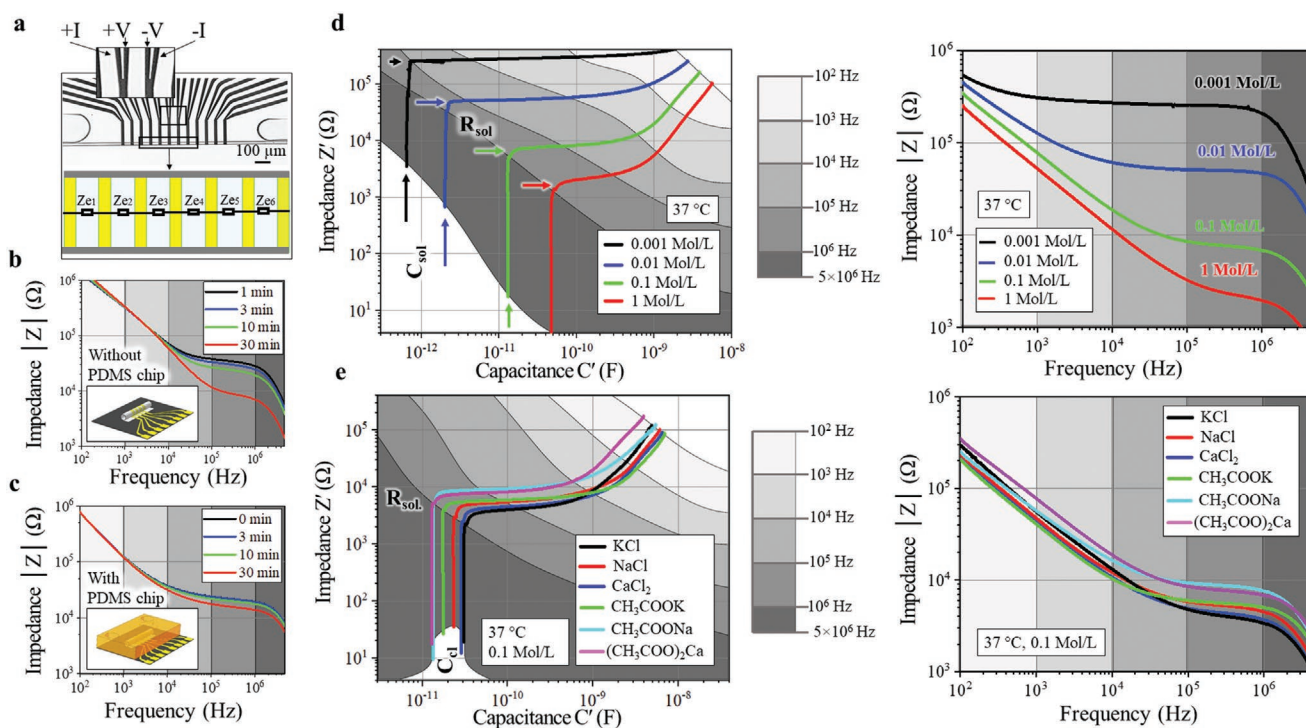


**Figure 3.** EIS chip calibration. a) Microscope image of rolled-up electrodes in a tube with an inner diameter of  $\approx 20 \mu\text{m}$  with a graphical representation of the embedded multigap electrodes. Bode plots for both b) open and c) encapsulated rolled-up electrodes. d) Changes in both impedance versus capacitance (left) and Bode impedance (right) plots of  $(\text{CH}_3\text{COO})_2\text{Ca}$  salt varying its concentration from 0.001 to 1 mol  $\text{L}^{-1}$ . e) impedance versus capacitance (left) and Bode impedance (right) plots of different ionic solutions under biological conditions ( $37^\circ\text{C}$ , 0.1 mol  $\text{L}^{-1}$ ).

continue with the characterization of our electrode system, we measured different ionic solutions containing sodium, potassium, calcium, chlorine, and acetate ions ( $\text{Na}^+$ ,  $\text{K}^+$ ,  $\text{Ca}^{2+}$ ,  $\text{Cl}^-$ , and  $\text{CH}_3\text{COO}^-$ ), typically present in living cells<sup>[37–39]</sup> over a concentration range from  $10^{-3}$  to 1 mol  $\text{L}^{-1}$ , and a temperature window from  $20^\circ\text{C}$  to  $47^\circ\text{C}$ . Such electrolytes produce ions in a concentration range from 0.001 to 0.1 mol  $\text{L}^{-1}$  which enables diverse cell functions (e.g migration, division, differentiation).<sup>[40]</sup> For this experiment, impedance spectra for each salt were obtained for frequencies ranging from 10 to  $5 \times 10^6$  Hz (Note S2, Supporting Information) using an Agilent 4294a impedance analyzer (see details in the Experimental Section). As the initial measurements were performed under static conditions, one key factor to consider is the evaporation of the analyte during the measurement time. For that, we carried out impedance measurements over a period of 30 min in both an open (Figure 3b) and closed environment (Figure 3c). As derived from the Bode plots, the open configuration leads to a faster solution evaporation, therefore a less reliable impedance signal, with a standard deviation of  $\pm 5 \times 10^4 \Omega$  after 30 min measurement. In contrast, the close configuration (embedding the electrodes in a microfluidic chip) is highly stable with a standard deviation of  $< 1 \times 10^4 \Omega$  (at least one order of magnitude lower) in the impedance signal after 30 min, making it suitable for further measurements.

Variations in impedance and capacitance as well as in the absolute impedance for each salt are observed for the encapsulated tubular sensor (Note S3, Supporting Information). We

analyzed the real part of the valued impedance and capacitance, as well as the Bode plots for different ionic solutions as shown in Figure 3d,e (left and right respectively). At lower frequencies and higher ionic concentrations, the surface roughness seems to play a substantial role leading to a strong frequency dependence of electrode–electrolyte interfacial capacitance and resistance in agreement with previous reports,<sup>[41]</sup> and which can be visualized in the equivalent circuit shown in Figure 4a and discussed in Note S4, Supporting Information.

In Figure 3d,e, a decrease in the solution resistance ( $R_{\text{sol}}$ ) and a simultaneous increase in the solution capacitance ( $C_{\text{sol}}$ ) is observed when increasing the ion concentration. Another factor that influences solution resistance and the double layer capacitance is the temperature, as high temperatures enhance ion mobility. We observe this effect in Figure S4a,b, Supporting Information, when the temperature is varied from  $20^\circ\text{C}$  to  $40^\circ\text{C}$  using a Peltier element located underneath the electrode system. We measured a decrease in both the real part of the impedance and of the capacitance, indicating a reduction of the overall system impedance due to the enhanced ion mobility, being more dominant at high salt concentration solutions.<sup>[42]</sup> As a consequence, it was important for our experiments to control the environmental conditions by avoiding medium evaporation and stabilizing the temperature in the physiological range ( $37^\circ\text{C} \pm 0.3^\circ\text{C}$ ) for all subsequent cell experiments. We also compared different salts at a fixed concentration (0.1 mol  $\text{L}^{-1}$ ) to evaluate the effect of ion content and mobility among the chosen salts (Figure 3e). As the temperature and concentration

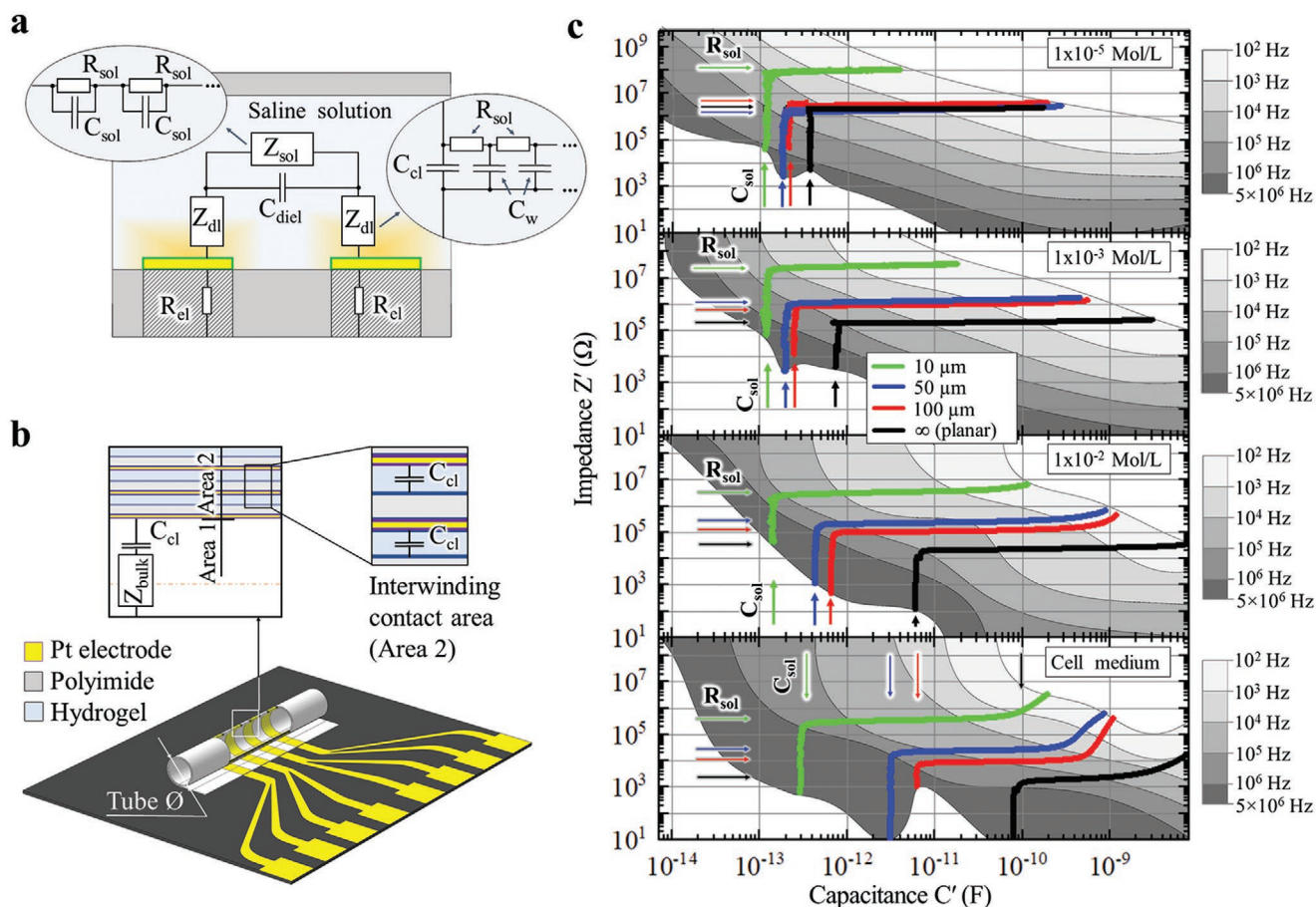


**Figure 4.** EIS characterization of tubular electrodes. a) Equivalent circuit for the measurement of ionic solutions. b) Sketch of tubular electrode capacitances in the tube and in the interwinding contacts. c) Real part of impedance versus real part of the complex capacitance plots as a function of tube diameter and salt concentration at room temperature.

was fixed, the variations of impedance are directly related to the ionic solution properties (ionic radius, mobility, and diffusion coefficient).<sup>[43]</sup> We clearly observed differences in both the real part of the impedance and of the capacitance when varying the electrolyte, in the frequency range from  $10^2$  to  $5 \times 10^6$  Hz. For example, KCl measurements show the lowest solution resistance compared to the other employed salts, probably due to its high ionic mobility.<sup>[44]</sup>

The electrodes were made in a “Swiss roll” like geometry with several tight windings (see inset in Figure 2b). The number of windings  $N_w$  is a function of the tube diameter  $\varnothing$  and the total rolling length  $L_r$  ( $N_w = L_r / \pi\varnothing$ ). Keeping  $L_r$  constant, the interwinding area increases with decreasing tube diameter. Thus, we not only consider the impedance from the contact between the electrolyte and the inner part of the tubular electrode, but also the impedances present in the interwinding space (Figure 4b). In Figure 4c, EIS characteristics are shown for tubes of different diameters compared to their planar counterparts. The first distinct feature is the increased  $R_{sol}$  with smaller tube diameter, which corresponds to a smaller bulk solution volume in the inner part of the tube. Likewise,  $C_{sol}$  shown in Figure 4c, corresponding to the solution capacitance, reduces with decreasing tube diameter. This happens because a larger area of the electrodes is constrained between the windings

(number of windings increases for the smaller tube diameter) and the hydrogel layer directly touches the electrode area. For the measured concentrations, the thickness of the solution ion diffusion layer ranges from few 10's nm to few  $\mu\text{m}$ 's<sup>[45]</sup> within the measured frequency range (further details are in Note S5 and Figure S5, Supporting Information). The direct contact between the electrode and the hydrogel reduces the value of  $C_{sol}$  and increases  $R_{sol}$  as the ionic mobility in the hydrogel is orders of magnitude lower compared to the liquid solution in the channel.<sup>[46]</sup>

It can also be seen from Figure 4c that smaller tubes possess almost the same  $C_{sol}$  among various ionic concentrations. The interwinding area of those tubes was almost completely covered by the hydrogel eliminating the surface electrode roughness effect. This effectively increases  $R_{sol}$  and reduces  $C_{sol}$ , eliminating the tail at low frequencies, in particular for small tubes. The area of the electrodes exposed to the electrolyte (the inner part of the tube) is reduced when decreasing the tube diameter, influencing the behavior of the capacitance at high frequencies. The capacitance increases with ionic concentration faster in the planar and large diameter (100  $\mu\text{m}$ ) tube cases, and remains almost constant for 10  $\mu\text{m}$  tubes due to the constraint of the electrodes between windings. Similarly, low frequency capacitances increase faster with concentration of the

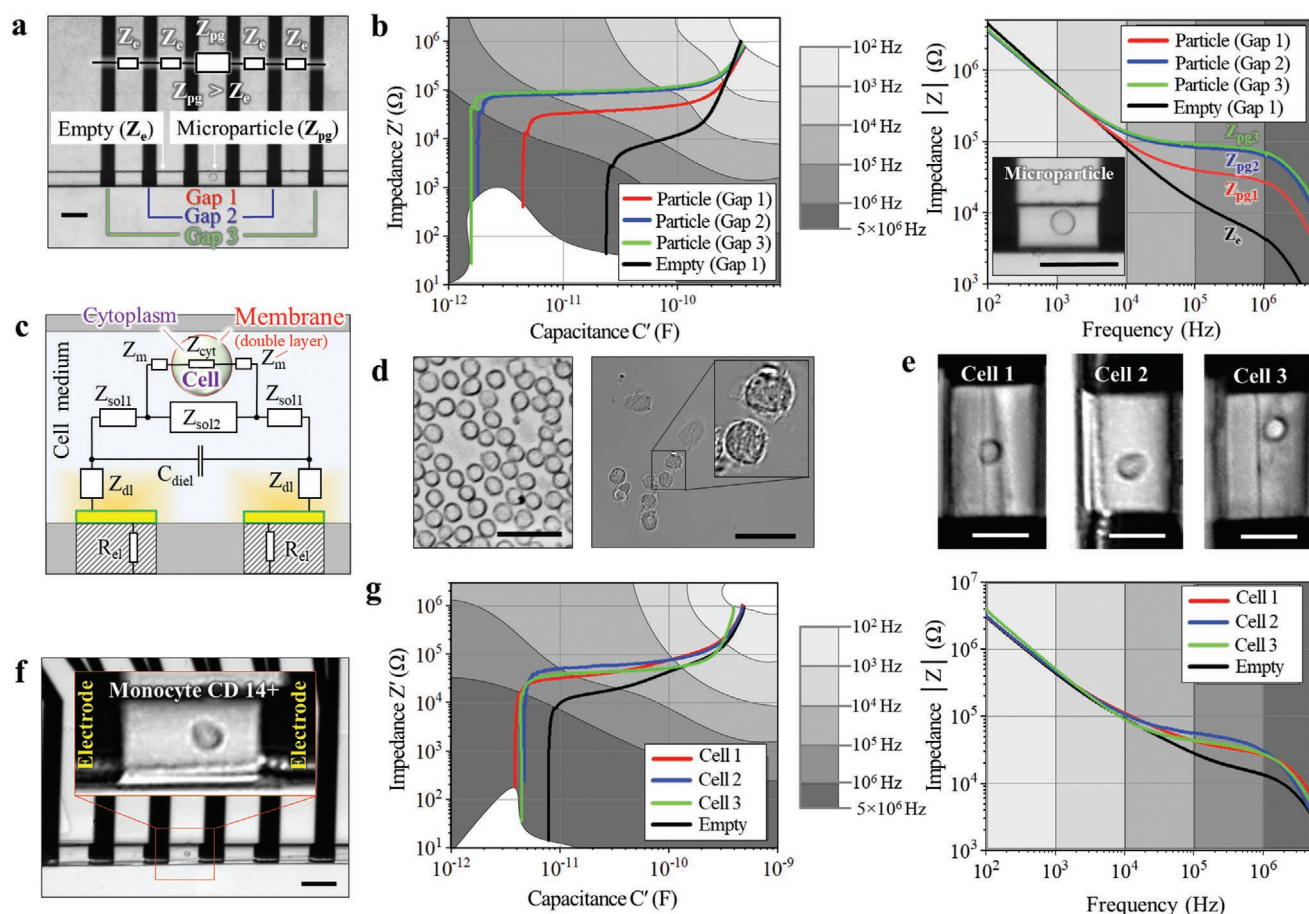


**Figure 5.** Micro objects (particles and cells) detection in static mode over the whole frequency range. a) Microscope image with integrated simplified equivalent circuit for the case of inserted particle. Scale bar is 50  $\mu\text{m}$ . b) Impedance versus capacitance plot (left) and Bode impedance plot (right) for the particle detection using three different gaps. Particle is in PBS 1X solution. Scale bar is 50  $\mu\text{m}$ . c) Detailed equivalent circuit for living cells passing through electrodes. d) General optical overview of monocytes CD14+. Scale bar is 50  $\mu\text{m}$ . e) Photo of three analyzed monocytes CD14+. Scale bar is 25  $\mu\text{m}$ . f) Microscope image of the cell inside the tubular electrode. g) Impedance versus capacitance plot (left) and Bode impedance plot (right) living single monocyte CD14+. Cells are in AB cell medium. Scale bar is 50  $\mu\text{m}$ .

solution for small tube diameters and remain almost constant in 50 and 100  $\mu\text{m}$  tubes where a large electrode area is exposed to the interior of the tube. Thus, to keep high impedimetric sensitivity to an analyzed sample (cells and expressed proteins) inside the channel, it is important to find a compromise between the object dimensions and low total impedance of the tubular sensor, by for example adjusting the tube diameter to the analyte sample size (e.g., microparticle or cell), and by performing the measurements with low conductivity electrolytes while maintaining cell viability.

Another parameter which should be considered is the distance between electrodes as the voltage drop along the channel is affected by such a separation and therefore its sensitivity to the measured object or cell in between. For example, a spherical 20  $\mu\text{m}$  polystyrene microparticle was introduced into a 25  $\mu\text{m}$  diameter tubular electrode with an array of parallel Pt electrodes (Figure 5a). The microparticle, as a homogeneous insulating spherical body, locally reduces the channel cross-section compared to the tube in the absence of the particle, reducing the effective electrolyte volume in between the electrodes (Figure 5b).<sup>[47–49]</sup> On the one hand, the absolute

impedance ( $Z_e$ ) (starting from  $10^4$  Hz) of the empty channel is smaller than the impedance of the channel with the inserted particle ( $Z_{pg}$ ), mainly caused by the reduced solution volume as mentioned above (see Figure 4c). On the other hand, when the distance between the electrodes increased, the impedance in each additional part of the sensing section (Figure S3, Supporting Information) becomes more dominant. For even larger gap distances ( $Z_{pg1}$ – $Z_{pg3}$ ), the solution resistance increases proportionally to the distance between the electrodes. Overall, the impedance is then limited by the high solution resistance and low capacitance of the narrow section, and changes proportionally with the distance between the electrodes. For analysis of particles and single cells, the shortest distance (gap 1–50  $\mu\text{m}$ ) is the most appropriate and therefore used for further investigations with cells inserted into the channel. Additionally, the cell medium was stabilized with (4-(2-hydroxyethyl)-1-piperazineethanesulfonic acid) (HEPES) (further details are in Note S6, Supporting Information) to prevent pH changes that may affect EIS signal. Furthermore, the temperature was set-up at 37  $^\circ\text{C}$  during all the measurements with a Peltier element.

The equivalent circuit of the pair of electrodes with a cell located in between, is depicted in Figure 5c, considering an already reported model for cells.<sup>[50]</sup> The suggested model considers the cell cytoplasm impedance ( $Z_{\text{cyt}}$ ), the cell membrane impedance ( $Z_{\text{m}}$ ), two areas with impedance of solution nearby the cell ( $Z_{\text{sol1}}$ ), and the impedance of the cell surrounding solution constrained by the channel diameter ( $Z_{\text{sol2}}$ ). Living monocytes CD14+ from human PBMCs suspended in cell medium were introduced into the tube (see Experimental Section). Monocytes have generally  $\approx 10\text{--}15\ \mu\text{m}$  in diameter before activation (Figure 5d). Once a cell reached the central position between two electrodes (Figure 5e,f), the EIS signal was immediately recorded, minimizing the influence of unspecific protein adsorption onto the electrode surface and avoiding attachment of the cell to the inner tube wall. The membrane impedance can be considered purely capacitive for living cells and is determined by the membrane capacitance, which is relatively small ( $0.7\text{--}12\ \mu\text{F cm}^{-2}$ ) compared to the double layer capacitance at biologically relevant ionic concentrations ( $>100\ \mu\text{F cm}^{-2}$ ).<sup>[49,51]</sup> This means that the accessible impedances are  $Z_{\text{sol1}} + Z_{\text{sol2}}$  which allows the determination of cell size as a ratio between  $Z_{\text{sol2}}$  and  $Z_{\text{sol1}}$ . The inserted cell displaces a part of the solution volume, which leads to an increase of  $R_{\text{sol}}$  and a decrease of  $C_{\text{sol}}$  within  $Z_{\text{sol2}}$  (Figure 5c). We measured three cells in the static regime confirming this behavior with small deviations related to variations in the shape/status of the cells (Figure 5g). From this measurement (Figure 5g), we selected the frequency range in which we observed the highest impedance change, when comparing empty and cell-filled electrodes. This frequency range between 10 and  $10^6$  Hz was selected for the following dynamic (in-flow) cell sensing experiments.

### 2.3. Monocytes CD14+ Detection and Analysis

As static measurements do not offer high throughput and require tedious cell micromanipulation, the subsequent measurements were carried out in flow by inserting a suspension of cells using a syringe pump at a constant flow rate of  $1.2 \times 10^{-5}\ \text{mL s}^{-1}$  (Figure 6a). In this way, the cells were precisely injected into the channel and detected at the selected frequencies. Videos S2, S3 and S4, Supporting Information, show the injection of monocytes CD14+ inside the microchannel in real time and their journey through the electrodes. The impedance was acquired continuously every 13 ms (Figure 6b,c). Whenever a cell passed through a pair of electrodes, an impedance peak occurred in the chronoimpedance plot. All changes in the cell metabolism resulted in differences in the ion environment of the cell medium (incubated externally, then fed into the EIS system), affecting equivalently  $Z_{\text{sol1}}$  and  $Z_{\text{bulk2}}$ . This allows for simultaneous characterization of the medium and its content such as cells, cell clusters, and fragments.<sup>[52]</sup> The corresponding impedance signal of single cells, cell clusters, and cellular fragments is represented in a cloud-like graph. In particular, the real and imaginary parts of the impedance and complex capacitance were directly extracted from the raw chronoimpedance data and plotted for two frequencies:  $10^5$  Hz and  $10^6$  Hz (Figure 6d,e). The absolute impedance of the single cell corresponds to  $\approx 37\ \text{k}\Omega$  at  $10^5$  Hz and  $\approx 24\ \text{k}\Omega$  at  $10^6$  Hz. For this

experiment, it was not necessary to do pre-sorting steps or elimination of cell fragments and clusters as required for regular cytometry. Instead, single cell signals are easily extracted by filtering out their corresponding impedance values. Thus, our system allows for carrying out measurements continuously and in-flow to collect information of a large number of cells. For example, cell fragments and single cells show lower impedance compared to cell clusters, thus they can be distinguished mainly due to their size differences.

As a next step, we performed LPS-induced monocytes CD14+ activation, and the EIS characterization in their medium within 24 h. In the previous section, we showed the characterization of the fabricated electrodes in various solutions (Figure S3c,d, Supporting Information) including cell medium, cell medium with HEPES, and cell medium with HEPES and LPS showing no substantial difference in the EIS signal, demonstrating the high stability and reproducibility of the measurement, allowing to distinguish slight changes promoted by the cell activation. LPS activation (mimicking the influence of foreign pathogens) induces a strong response from the immune system monocytes. The activation of human monocytes CD14+ occurs due to the LPS interaction with the acute-phase protein and LPS-binding protein. The LPS–LPS-binding protein complex connects to the toll-like receptor (TLR), resulting in a cellular activation expression of signaling proteins – pro- and anti-inflammatory cytokines.<sup>[23,53]</sup> The expressed cytokines are then released to the cell surrounding medium as well as accumulated by adsorption on the sensor surface (electrode, inner walls of polymeric tube, and even PDMS connector with flexible tubing). The adsorption happens due to different non-covalent interactions that occur between the protein-surface such as the intermolecular forces of van der Waals, hydrophobic and electrostatic interactions, and is often related to formation of monolayers, that leads to change impedance.<sup>[54,55]</sup>

The proposed sensor-in-a-tube is able to record simultaneously the signal from individual cells passing through the electrode as well as the extracellular medium conductivity (which varies according to the expressed cytokines, metabolism products, and release of intracellular medium ions) upon different activation times.<sup>[56,57]</sup> However, with the current platform, it is not possible yet to distinguish between the different cytokines or metabolism products present in the extracellular medium. The detection of single cells results in well-defined peaks on the chronoimpedance plot. The peak amplitude and width depend on whether a single cell, a cluster of cells or sample debris is detected. In contrast, the expressed cytokines, ions, and metabolism products in the extracellular matrix affect the baseline of the impedance response. Some of these molecules presumably accumulate on the electrode surface which can be observed at lower frequencies, while at higher frequencies, bulk properties of fluids, cellular membrane, and cytoplasm play a dominant role.

Exemplary microscope images in Figure 7a, inset show cell morphological changes during different activation times with maximum variations observed at 6 and 24 h. There is no significant difference in cell morphology during the first 3 h after activation in agreement with previous studies.<sup>[58]</sup> After 6 h, activated cells showed a size increase as well as a formation of specific “dendritic-like” structures which are typically associated

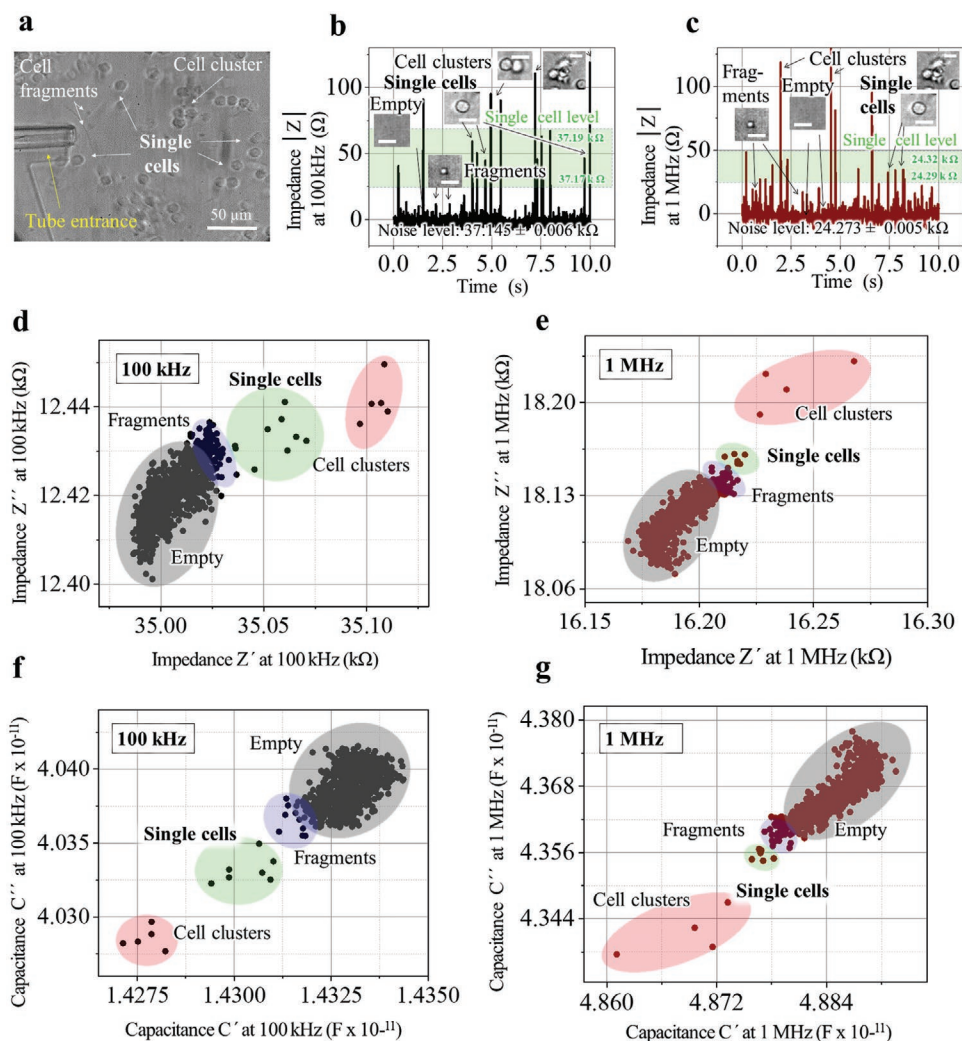


**Figure 6.** In-flow monocytes CD14<sup>+</sup> chronoimpedance. a) Microscope images of cell suspension near the tube entrance. b) Absolute impedance versus time at  $10^5$  Hz. Scale bars are 20  $\mu\text{m}$ . c) Absolute impedance versus time at  $10^6$  Hz. Scale bars are 20  $\mu\text{m}$ . d) Complex impedance cloud plot representation of Figure 6b. e) Complex impedance cloud plot representation of Figure 6c. f) Complex capacitance cloud plot representation of Figure 6b. g) Complex capacitance cloud plot representation of Figure 6c. All results are based on dynamic measurements of cell suspension over 30 s at room temperature in constant flow rate  $1.2 \times 10^{-5}$   $\text{mL s}^{-1}$ .

with active cytokines expression.<sup>[59–61]</sup> After 24 h, activated cells exhibited more pronounced changes in their cell morphology such as shrinking and loosening of their membrane integrity, probably due to the initiation of necrosis or apoptosis processes.<sup>[62,63]</sup> LPS treatment of monocytes was performed in a standard well plate, under physiological incubation conditions, where  $\approx 60$ – $70\%$  of cells remained viable after 24h of LPS-mediated activation. (Figure S7, Supporting Information). Most of the dead cells can be found in big clusters or being fragmented. Cells were injected inside the chip during measurements for only 1 min including preparation steps, reducing the influence of the manipulation or chip handling on the cell viability. The cells were located inside the tubular sensor for only few ms for EIS signal detection. The fluidic chip was thermally stabilized and encapsulated so that the liquid did not evaporate (see Experimental Section). In Figure 7b, we plotted the impedance signal of  $\approx 30$  single cells from the chronoimpedance plot

as well as 30 measurement points corresponding to “empty” cell medium (without cell). The selection of single cells from the flow was carried-out with conventional optical microscope allowing to correlate single cells and the EIS signal. We collected impedance data over 30 s (4 s is shown in Figure 7a) during which the flow and concentration of cells was stable. A variation in the baseline of the impedance characteristics was observable in the chronoimpedance plots (Figure 7a), which we attribute to the activation states of the cells. The impedance baseline was measured in the range of 143–152  $\text{k}\Omega$ . At the maximum of LPS activation (starting at  $\approx 6$  h), the impedance decreases to  $\approx 40$   $\text{k}\Omega$  indicating an increase of conductivity due to the presence of large amounts of metabolism products as well as expressed cytokines in the surrounding cell medium. A slight decrease of the baseline has been observed after 24 h, which we attribute to the cytoplasm released during apoptosis or necrosis of cells. The clouds in the impedance (Figure 7b)

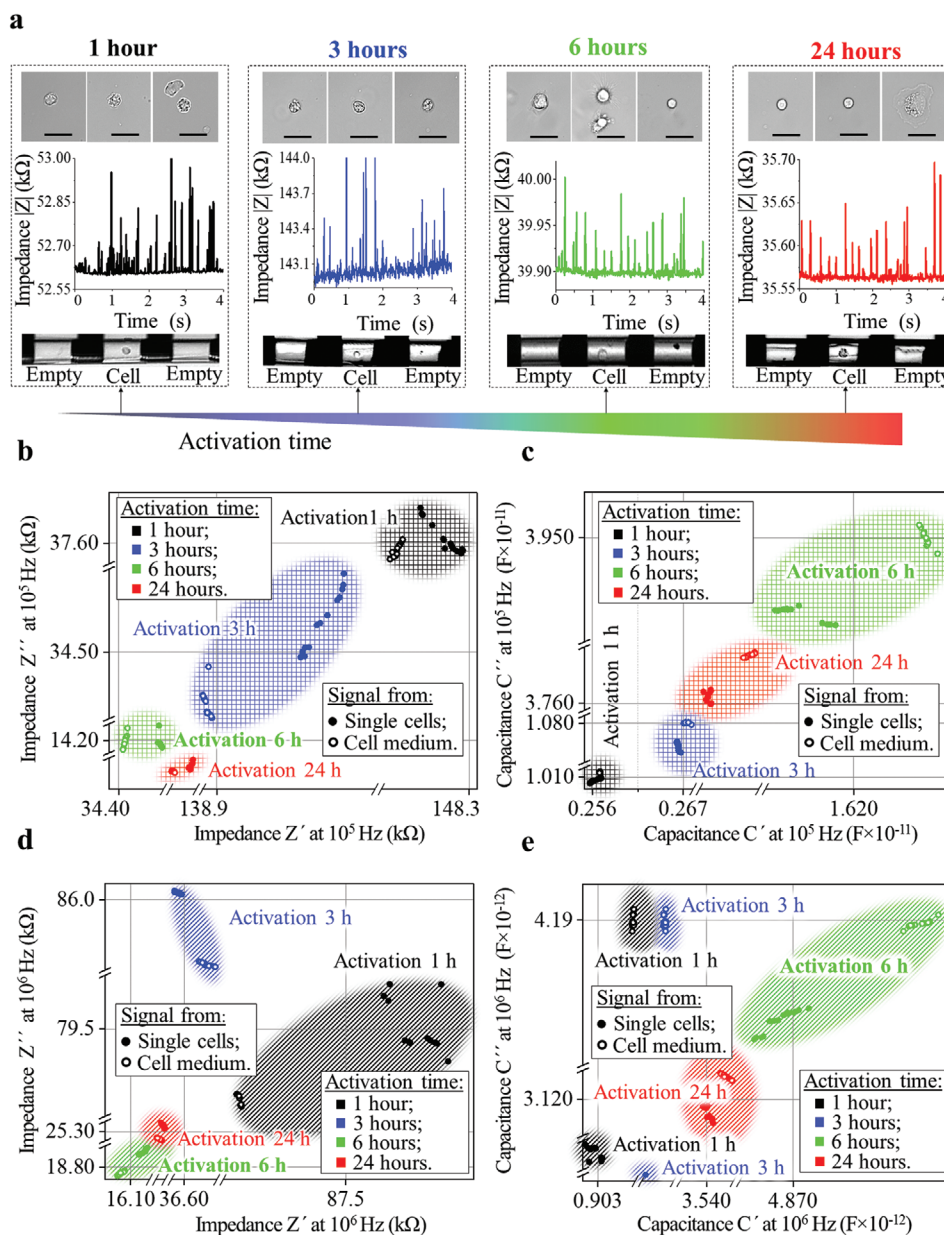


**Figure 7.** In-flow monocytes CD14<sup>+</sup> analysis at 10<sup>5</sup> and 10<sup>6</sup> Hz. a) Morphological overview of monocytes activated for 1, 3, 6, and 24 h with corresponding absolute impedance plot versus time. Scale bars are 20  $\mu$ m. b) Cloud impedance plot of activated cells and surrounding cell medium at 10<sup>5</sup> Hz. c) Cloud complex capacitance plot of activated cells and surrounding cell medium at 10<sup>5</sup> Hz. d) Cloud impedance plot of activated cells and surrounding cell medium at 10<sup>6</sup> Hz. e) Cloud complex capacitance plot of activated cells and surrounding cell medium at 10<sup>6</sup> Hz.

and capacitance (Figure 7c) plots measured at 10<sup>5</sup> Hz demonstrate significant differences for all activation time steps. Here, impedance decreases continuously with time. In particular, the imaginary part of the impedance related to the double layer and solution capacitances decrease upon increasing activation time, while the real part of the impedance seems to slightly increase after 24 h activation time. The latter might be due to the unspecific attachment of remaining cell proteins and biomolecules onto the electrode surface after cell apoptosis/necrosis, hindering the electron transfer from the electrolyte to the electrode surface (Figure 7b). The corresponding capacitance signal can

be better visualized in Figure 7c, agreeing with the impedance cloud plots as explained above. Any accumulation of cell debris was not observed onto electrodes during measurements as the high flow serves to renew the analyte, cleaning the electrode surface. Similar measurements of impedance and capacitance were performed at 10<sup>6</sup> Hz (Figure 7d,e), revealing a strong increase of the imaginary part of the impedance and capacitance after 1 and 3 h activation. This increase in solution capacitance might be caused by ion release into the cell surrounding medium and therefore increase of  $Z_{sol1}$  prior to the LPS induced activation.

## 2.4. Cytokine Analysis

Recent studies have shown a significant increase of cytokine expression in the surrounding medium for LPS stimulated human monocytes, especially of TNF- $\alpha$  (up to 3 ng mL<sup>-1</sup>) and IL-6 (up to 0.5 ng mL<sup>-1</sup>), after 6 h of LPS (10 ng mL<sup>-1</sup>) activation.<sup>[60]</sup> Increased amounts of LPS (1  $\mu$ g mL<sup>-1</sup>) result in an increasing of expressed cytokines: TNF- $\alpha$  (up to 13 ng mL<sup>-1</sup>) and IL-6 (up to 7.5 ng mL<sup>-1</sup>), after 12 h of activation and a subsequent reduction of cytokine concentration starting at 20 h.<sup>[64–66]</sup> In this work, we applied LPS (100 ng mL<sup>-1</sup>) activation, an intermedium concentration from the reported literature, and according to protocols developed in University Hospital Carl Gustav Carus at Dresden University of Technology.

In the previous section, we evaluated the overall influence of all expressed cytokines, ions release, and metabolism on the cell medium conductivity over different activation times, but it was not possible to discriminate each individual cytokine. In order to further understand the influence of individual cytokines on the sensor EIS response, we prepared spiked solutions, employing cell medium containing the following cytokines: TNF- $\alpha$ , IL-1 $\beta$ , IL-6, IL-10, IL-12 (prominent markers in immune diseases diagnosis). The chosen concentration range was from 1 to 5 ng mL<sup>-1</sup>, in the range of previously reported data (details are described in the Experimental Section). With the developed sensor, the minimum detectable concentration of an exemplary cytokine TNF- $\alpha$  was 10<sup>-8</sup> pg mL in DI water. When using a

biorelevant fluid as cell medium, which has high ionic strength, the minimum detectable concentration reduces  $\approx$ three orders of magnitude. The sensor remains sensitive at least until concentration 500 ng mL<sup>-1</sup>. Future information can be found in Figures S8 and S9 and in Note S7, Supporting Information, revealing nonlinear concentration dependences of EIS signal.

The impedance cloud plot at 10<sup>5</sup> Hz in Figure 8a reveals a decrease in the impedance signal at 2.5 ng mL<sup>-1</sup> cytokine concentration compared to 1 ng mL<sup>-1</sup>. In contrast, at higher cytokine concentrations ( $\approx$ 5 ng mL<sup>-1</sup>), the impedance increases. This behavior was observed for all cytokines in the same concentration range. In contrast, the capacitance shows the opposite behavior (Figure 8b), meaning an increase of capacitance upon an increase of cytokine concentration (up to 2.5 ng mL<sup>-1</sup>) and a decrease of the capacitance if the concentration increased up to 5 ng mL<sup>-1</sup>. This behavior was observed for the six different selected cytokines, based on 800 points of measurements, with a standard deviation maximum of 200  $\Omega$ . The increased impedance at higher cytokines concentration spiked samples might be due to an increase in the overall electrolyte conductivity that influences the double layer capacitance screening the ion transfer to the electrode. Further studies need to be pursued to learn more about the exact contribution of individual cytokines on the sensor response and their correlation to the different cell activation steps.

The clear dependence of impedance (Figure 8a) and capacitance (Figure 8b) signals on cytokine concentrations was

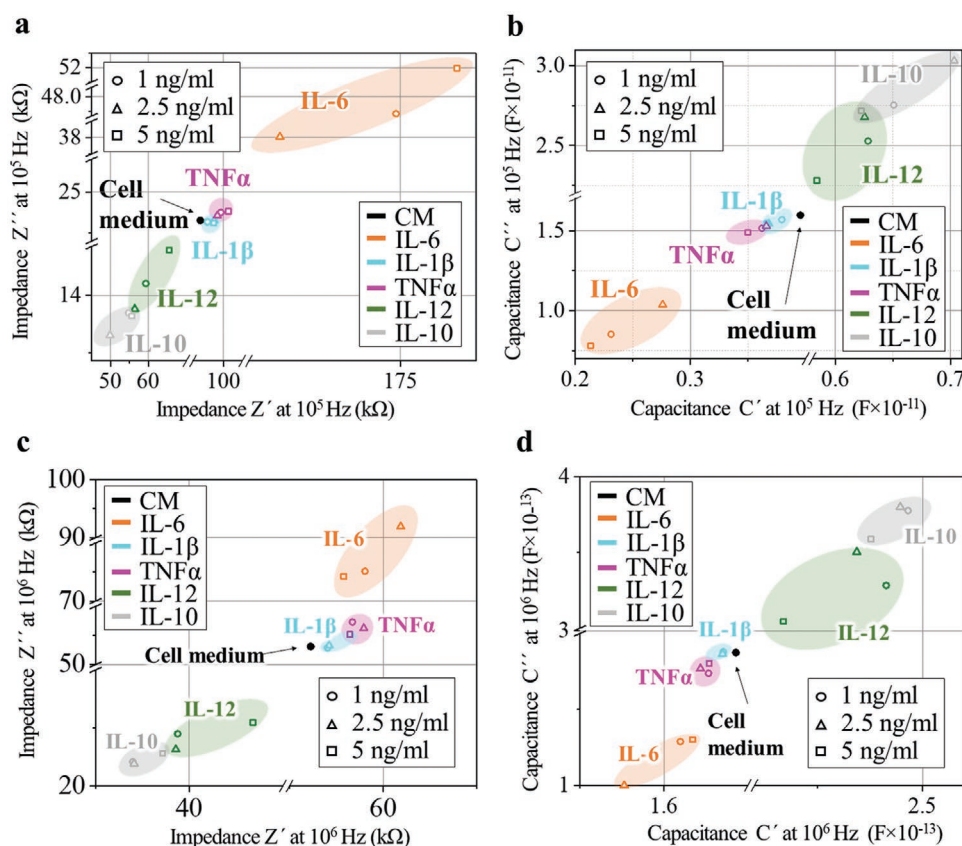


**Figure 8.** In-flow cytokines analysis at 10<sup>5</sup> and 10<sup>6</sup> Hz. a) Cloud impedance plot of cytokines at 10<sup>5</sup> Hz. b) Cloud complex capacitance plot of cytokines at 10<sup>5</sup> Hz. c) Cloud impedance plot of cytokines at 10<sup>6</sup> Hz. d) Cloud complex capacitance plot of cytokines at 10<sup>6</sup> Hz.

observed for all investigated cytokines and has the similar trend as for LPS activated monocytes (see Figure 7). The absolute impedance after 24 h activation drops mainly due to the fact that most of the cells are in the necrosis or apoptosis stage, causing an increase of solution conductivity due to more ionic charges in the solution (from the cell cytoplasm).

Similar trends of decreasing impedance signal and increasing capacitance with increasing concentrations from 1 to 2.5 ng mL<sup>-1</sup> were observed for IL-10 and IL-12 (Figure 8c,d). TNF- $\alpha$ , IL-1 $\beta$ , IL-6 exhibit an increase of capacitance and a decrease of impedance at the maximal concentration (5 ng mL<sup>-1</sup>). Thus, the measurement of cell suspension at different excitation frequencies will allow future identification of single cytokines by analyzing their individual response at a selected frequency corresponding to  $R_{sol}$  and  $C_{sol}$  sensitivity.

All analyzed EIS plots for spiked-cytokine solutions demonstrate a clear dependence of impedance and capacitance on cytokine concentration. However, the identification and quantification of single biomolecules from this kind of mixtures is limited in the current conventional linear EIS, especially if no functionalization or labeling procedures are employed. In unknown mixtures, a possible solution for improving the sensor selectivity in a label and functionalization-free fashion would be the use of nonlinear EIS. The nonlinear response (e.g., harmonics and mixing products) would effectively separate the molecular response signal from a bulk signal (ionic solutions in biological assays), enabling the analysis of cytokines with higher sensitivity and selectivity. Addressing nonlinear properties (conductivity, permittivity, and dielectric loss) of such liquids and the parameterization of their response functions would provide a parameter space of sufficient dimensionality for the differentiation of each individual cytokine as well as their concentration in complex biological solution. Using nonlinear identification methods combined with conventional EIS would be the powerful solution to develop future type of label-free specific impedimetric sensors. However, it is not shown in this work as the complete hardware and software require further optimization and the interpretation of data is not so straightforward and dedicated algorithms need to be developed.

### 3. Conclusion

We have introduced a novel label-free impedimetric sensor-in-a-tube for simultaneous single immune cell and extracellular medium analysis. The platform is based on a self-assembled strained polymeric layers, containing Pt electrodes which can be reproduced with a yield of  $95.2 \pm 4\%$  on wafer scale. The fabricated rolled-up microtubes had a length of 10 mm and diameters ranging from 20 to 120  $\mu\text{m}$  integrating a linear array of electrodes. Electrical impedance spectroscopy in a frequency range from  $10^2$  to  $5 \times 10^6$  Hz was performed in order to analyze biologically-relevant ionic solutions and characterize the electrode system to select the proper detection parameters. Platinum-based electrodes were used due to their high polarization and good reversibility properties.

The influence of the sensor geometry on the EIS response, when measuring different biologically-relevant ionic solutions

(KCl, NaCl, CaCl<sub>2</sub>, CH<sub>3</sub>COOK, CH<sub>3</sub>COONa, (CH<sub>3</sub>COO)<sub>2</sub>Ca) was analyzed for both tubular and planar electrodes in a concentration range from  $1 \times 10^{-5}$  to 1 mol L<sup>-1</sup>. Moreover, measurements of ionic liquids were carried out, revealing a high sensitivity to ionic concentration when decreasing the diameter of the sensor-in-a-tube. The measurements were performed in static and dynamic modes for both monocytes CD14+ cells and their surrounding medium with an analysis speed of  $1.2 \times 10^{-5}$  mL s<sup>-1</sup> without involving the use of sorting or pre-selecting modules as employed in conventional cytometers. We also demonstrated the use of the sensor-in-a-tube system as a cell counter, enabling the signal discrimination of single cells, cell clusters, and fragments.

Lipopolysaccharide (LPS) induced activation of monocytes CD14+ was analyzed, focusing on the impedance changes after different activation time points by EIS, correlated to optical morphological analysis. The maximum difference in cell morphology and impedance signal was observed at 6 h (increase of cell size and form changes) and 24 h (cell shrink). The maximum capacitance and decreased impedance at 6 h indicated a probable increase of metabolism products and expressed cytokines in the extracellular medium at both (10 and 10<sup>6</sup> Hz) excitation frequencies.

The sensor-in-a-tube was able to detect individually TNF- $\alpha$ , IL-1 $\beta$ , IL-6, IL-10, and IL-12 cytokines in a concentration range of 1, 2.5, and 5 ng mL<sup>-1</sup> in spiked solutions. However, in the present work we have achieved a minimum detectable concentration of  $10^{-5}$  pg mL<sup>-1</sup> for cytokines typically expressed by monocytes CD14+ upon LPS-mediated activation for the biorelevant conditions.

The developed platform represents a novel strategy for high throughput single immune cell sensing combining simultaneous analysis of cells and their extracellular medium without labeling and surface functionalization. Still further studies need to be pursued in order to resolve individual cytokines from the whole cell surrounding medium and to be able to correlate them with different cell status which allows in future to perform a personalized and accurate immune disease diagnosis in a simple manner.

### 4. Experimental Section

*Treatment of the Glass Substrate Surface:* Cover glass with dimensions of  $100 \times 100 \times 1$  mm<sup>3</sup> were used as a substrate for the polymeric stack deposition. Initially, the glass substrates were washed in the Steelco DS500 (STEELCO S.p.A.) washing machine using neodisher LaboClean FM (Dr. Weigert GmbH & Co.) and then neutralized with neodisher Z (Dr. Weigert GmbH & Co.). For better adhesion of the polymeric layers, the glass surface was modified for 20 min by mono-layer of 3-(trimethoxysilyl) propyl methacrylate (Polysciences Europe GmbH, Eppenheim,) using recently reported method.<sup>[67]</sup>

*Polymer Stack Fabrication:* The synthesis of polymeric layers was based on the already reported technology of strained polymeric layers assembly.<sup>[33]</sup> The stack of polymer layers was successively deposited onto a cover glass slide. First, the sacrificial layer (SL) prepared from acrylic acid (AA) and hydrated LaCl<sub>3</sub> (Alfa Aesar) was spin-coated at 3000 r.p.m for 35 s without further purification to produce a 500-nm thick layer. The patterning of polymer layers was done using the standard mask aligner SUSS MA4 through glass/Cr mask and rinsed in deionized (DI) water. The sample was exposed to a 405 nm mercury h-line (20 mW cm<sup>-2</sup>).

Finally, the polymer layer was annealed at 220 °C for 5 min under nitrogen atmosphere to remove all solvent residuals.

Then, the synthesized hydrogel (HG) as an active (swelling) layer was successively spin-coated onto dry SL surface at 7000 r.p.m for 60 s to produce a 150-nm thick layer. After drying, the HG layer was exposed for 60 s with mask aligner, developed in Diethylene glycol monoethyl ether (Sigma–Aldrich) and baked at 220 °C for 5 min under nitrogen atmosphere.

Finally, the polyimide (PI) was deposited as the passive layer onto the HG surface by spin-coating at 5000 r.p.m. for 35 s to have a 450-nm thick layer. After drying, the PI layer was exposed for 90 s and developed in NEP-based solvent and hard-backed at 220 °C for 10 min.

Every deposition step was finished by the controlling of final polymeric layer thickness by Stylus Profilometer (Dektak, Bruker) and quality of fabricated films by Axioscope A1 microscope (Zeiss corp.). The spin-coating parameters varied to obtain a layer thickness corresponding to the specific tube inner diameters from 15 to 800  $\mu\text{m}$  (Figure 1) and reach programmable mechanical properties, for example, deformation (Figure S2, Supporting Information).

**Fabrication of the Sensing Electrodes on the Planar Arrangement:** Conductive electrode layer consisting of Cr (10nm)/Pt (100nm) was deposited via electron beam evaporation (base pressure:  $1 \times 10^{-6}$  bar; deposition rate:  $2 \text{ \AA s}^{-1}$ ). The width of the electrode was 30  $\mu\text{m}$  with the interspace of 50  $\mu\text{m}$ . The metal deposition was realized using standard UV lithography by lifting-off the underlying AZ5214E photoresist (Micro Chemicals) layer.

**Self-Assembly Process into Tubular Architecture:** The planar layouts were self-assembled into 3D self-rolled structures by selectively etching the sacrificial layer in a solution of 0.5 M sodium diethylenetriaminepentaacetic acid (DTPA pH 4–8) (Alfa Aesar, UK) and rinsed in DI water after the rolling process is complete. Then, the samples were transferred into the saturated Camphor 98% (Alfa Aesar) solution in acetone and slowly pulled out from this solution to obtain a Camphor layer on the whole sample surface. Finally, the samples were dried under the room conditions during 24 h for complete camphor evaporation from the surface resulting in fixation of completely dried self-rolled tube in rolled state.

**Microfluidic Integration:** Specially designed channels for microfluidic integration were prepared from PDMS (Sylgard 184 silicon elastomer kit, The Dow Chemical Company) mixed in proportion 1:10 (curing agent: elastomer base) with standard soft lithography process<sup>[34]</sup> onto the SU-8 50 (Micro Chemicals Corp.) master and were cut with a blade. The holes for external tube connections were made in PDMS channel using Rapid-Core hole puncher (Science Service). After cutting and detaching from the master, the contact surfaces of PDMS channels and glass substrate for the samples were oxidized in Femto plasma generator (Diener electronics) for 30 s. Then, the PDMS channel was precisely positioned on the sample by the SUSS MA4 mask aligner, close contact established between each together and heated at 100 °C on the hot-plate for 5 min in order to create an irreversible covalent bonding and ensure hermetic connection (Figure S1b, Supporting Information).<sup>[35]</sup> Finally, the self-rolled tube inside the PDMS channel was sealed with liquid PDMS using lateral filling channels and heated at 150 °C for 5 min to cross-link liquid PDMS. The external BOLA PTFE tubing ID 0.3mm, OD 0.6mm (Sigma–Aldrich) were connected to the neMESYS syringe pump (CETONI comp.) for the precise flow control inside the self-rolled tube.

**Sensor Calibration:** To calibrate the sensor response to multiple concentration and temperature changes, the following ionic solutions in DI water were prepared in the concentration range 0.0001, 0.001, 0.01, 0.1, and 1 mol L<sup>-1</sup>: KCl, NaCl, CaCl<sub>2</sub>, CH<sub>3</sub>COOK, CH<sub>3</sub>COONa, and (CH<sub>3</sub>COO)<sub>2</sub>Ca (Sigma–Aldrich). These solutions were injected through the sensor at flow rate 10  $\mu\text{L min}^{-1}$  and the flow was stopped during the measurement. The tube was washed with DI water five times between changing of ionic solution. Temperature controlling of sensor was realized using a compact Peltier element inserted in the sample holder and contacting directly to the bottom side of sensor substrate.

To calibrate sensor response to microobjects, for example, particles and cells inside sensing area, the spherical 20  $\mu\text{m}$  polystyrene

microparticles (Supelco) were introduced inside the sensor by the micromanipulator installed on the Axio cell observer Z1 (Zeiss corp.). The solution was PBS 1X. In case of selecting signal of living cells from chronoimpedance, we collected impedance data over 10 s during which the flow and concentration of cells was stable. During this time, we collected signals from solution and all types of objects dispersed in the solutions including fragment, cells, and cellular clusters. Only signals corresponding to single cells were selected from chronoimpedance and represented in Figures 6 and 7 in the manuscript. Signals from cluster of cells and cell fragments forming the majority of the spikes within the acquired data, were not analyzed. The calibration of the impedance signal and selection of single cells was carried out with a standard optical microscope.

**Cell Culture:** The living cells (monocytes CD14+) were provided by Universitätsklinikum Carl Gustav Carus Dresden and were sorted according to the protocol given for the Easy Sep Human Monocyte Isolation Kit (Stemcell Technologies). Then cells were in ice until cultivation about 2–3 h. Cells were seeded out in 96 well plates with rounded bottom (Thermo Scientific) (200  $\mu\text{L}$  cell suspension per well) with AB cell medium and were cultured overnight at 37 °C  $\pm$  0.3 and 5% CO<sub>2</sub>. Activation process started the next day by adding an LPS solution (100 ng mL<sup>-1</sup>) and keeping in the incubator during the activation time. After stimulation, cells were put in ice for 30 min and then pooled and transferred into a 15 mL tube. 9 mL of PBS was added into the tube and it was centrifuged (Centrifuge 5430 R, Eppendorf) at 250  $\times$  g; 4 °C for 10 min. Then, the supernatant was removed and cells were resuspended in 0.5 mL cell medium. Finally, 10  $\mu\text{L}$  4-(2-hydroxyethyl)-1-piperazineethanesulfonic acid (HEPES) buffer (Thermo Fisher Scientific) per 500  $\mu\text{L}$  medium (20 mM HEPES) was added to stabilize cell medium maintaining physiological pH and preventing oxidation process.

**Cytokines Preparation:** Cytokines were prepared from ELISA kit (Thermo Fisher Scientific) according to the preparation manual. Analyzed cytokine solutions were diluted in AB cell medium in concentration of 1 to 5 ng mL<sup>-1</sup> and stored in the fridge at  $+5 \pm 0.5$  °C during 3 h.

**Electrical Impedance Spectroscopy:** EIS measurements were carried out by 4294A precision impedance analyzer (Keysight technologies) in a frequency range  $10^2$ – $5 \times 10^6$  Hz with signal of 500 mV. Connection to the sensor electrodes was realized by 4-probes method with Cascade Microtech DCP 100 probes (FormFactor) on the PSM 6 wafer probe station (Karl Suss). The external temperature during the measurements was kept at 37 °C. Dynamic (in-flow) cell and cytokines measurements were carried out at selected frequencies ( $10^4$  and  $10^5$  Hz) with the smallest gap (50  $\mu\text{m}$ ) in constant flow  $1.2 \times 10^{-5}$  mL s<sup>-1</sup>. Total EIS signal from cytokines spiked solutions was a mean of 800 single measurements for each cytokine at single selected frequency with standard deviation maximum 200  $\Omega$ .

## Supporting Information

Supporting Information is available from the Wiley Online Library or from the author.

## Acknowledgements

The work was financially supported by the German Research Foundation DFG SPP 1857 ESSENCE grant (KA5051/1-1 and ME4868/2-1). O.G.S. acknowledges financial support by the Leibniz Program of the German Research Foundation (SCHM 1298/26-1). O.G.S. and M.M.-S. also acknowledge the support from the European Union's Horizon 2020 research and innovation program under the grant agreement nos. 835268 and 853609, respectively. The authors acknowledge the Neuroimmunological laboratory of Clinic and Polyclinic for Neurology at University Clinique Carl Gustav Carus Dresden for their help with biological materials manipulations. The support of the clean room team headed by R. Engelhard (IIN/IFW Dresden) and the assistance

in development of the experimental setups by the research technology department of IFW Dresden is greatly appreciated. The authors further thank C. Krien and I. Fiering (IIN/IFW Dresden) for the deposition of metallic thin films, Sonja M. Weitz, and S. Baunack (IIN/IFW Dresden) for FIB/SEM analysis.

Open access funding enabled and organized by Projekt DEAL.

## Conflict of Interest

The authors declare no conflict of interest.

## Keywords

electrical impedance spectroscopy, label-free sensor, lab-in-a-tube, shapeable materials technologies, single-cell analysis

Received: April 22, 2020

Revised: November 12, 2020

Published online: January 15, 2021

- 
- [1] J. R. Miller, *J. Managed Care Pharm.* **2004**, *10*, S4.
- [2] S. Lohi, K. Mustalahti, K. Kaukinen, K. Laurila, P. Collin, H. Rissanen, O. Lohi, E. Bravi, M. Gasparin, A. Reunanen, M. Mäki, *Aliment. Pharmacol. Ther.* **2007**, *26*, 1217.
- [3] M. Versini, P. Jeandel, E. Rosenthal, Y. Shoenfeld, *Autoimmun. Rev.* **2014**, *13*, 981.
- [4] A. Lerner, P. Jeremias, T. Matthias, *Int. J. Celiac Dis.* **2015**, *3*, 151.
- [5] J. C. Martin, D. E. Swartzendruber, *Science* **1980**, *207*, 199.
- [6] J. P. Nolan, L. A. Sklar, *Nat. Biotechnol.* **1998**, *16*, 633.
- [7] P. O. Krutzik, G. P. Nolan, *Nat. Methods* **2006**, *3*, 361.
- [8] J. Wang, D. Karnaushenko, M. Medina-Sanchez, Y. Yin, L. Ma, O. G. Schmidt, *ACS Sens.* **2019**, *4*, 1476.
- [9] P. Pozarowski, E. Holden, Z. Darzynkiewicz, *Methods Mol. Biol.* **2013**, *931*, 187.
- [10] T. Ichimura, L. Da Chiu, K. Fujita, H. MacHiyama, T. Yamaguchi, T. M. Watanabe, H. Fujita, *Sci. Rep.* **2016**, *6*, 37562.
- [11] A. Ramoji, O. Ryabchykov, K. Galler, A. Tannert, R. Markwart, R. P. Requardt, I. Rubio, M. Bauer, T. Bocklitz, J. Popp, U. Neugebauer, *ImmunoHorizons* **2019**, *3*, 45.
- [12] C. S. Bausch, C. Heyn, W. Hansen, I. M. A. Wolf, B. P. Diercks, A. H. Guse, R. H. Blick, *Sci. Rep.* **2017**, *7*, 41584.
- [13] U. S. Eggert, T. J. Mitchison, *Curr. Opin. Chem. Biol.* **2006**, *10*, 232.
- [14] Z. E. Perlman, M. D. Slack, Y. Feng, T. J. Mitchison, L. F. Wu, S. J. Altschuler, *Science* **2004**, *306*, 1194.
- [15] J. Chen, C. Xue, Y. Zhao, D. Chen, M. H. Wu, J. Wang, *Int. J. Mol. Sci.* **2015**, *16*, 9804.
- [16] F. Radford, S. Tyagi, M. L. Gennaro, R. Pine, Y. Bushkin, *Crit. Rev. Immunol.* **2016**, *36*, 359.
- [17] F. Fasbender, C. Watzl, *Sci. Rep.* **2018**, *8*, 4938.
- [18] A. Baraket, M. Lee, N. Zine, N. Yaakoubi, M. G. Trivella, A. Elaissari, M. Sigaud, N. Jaffrezic-Renault, A. Errachid, *Sens. Transducers J.* **2014**, *27*, 15.
- [19] X. Li, M. Soler, C. Szydzik, K. Khoshmanesh, J. Schmidt, G. Coukos, A. Mitchell, H. Altug, *Small* **2018**, *14*, 1800698.
- [20] K. Bhavsar, A. Fairchild, E. Alonas, D. K. Bishop, J. T. La Belle, J. Sweeney, T. L. Alford, L. Joshi, *Biosens. Bioelectron.* **2009**, *25*, 506.
- [21] P. A. Scherle, E. A. Jones, M. F. Favata, A. J. Daulerio, M. B. Covington, S. A. Nurnberg, R. L. Magolda, J. M. Trzaskos, *J. Immunol.* **1998**, *161*, 5681.
- [22] V. Seow, J. Lim, A. Iyer, J. Y. Suen, J. K. Ariffin, D. M. Hohenhaus, M. J. Sweet, D. P. Fairlie, *J. Immunol.* **2013**, *191*, 4308.
- [23] R. E. Plevin, M. Knoll, M. McKay, S. Arbabi, J. Cuschieri, *Shock* **2016**, *45*, 22.
- [24] J. T. La Belle, K. Bhavsar, A. Fairchild, A. Das, J. Sweeney, T. L. Alford, J. Wang, V. P. Bhavanandan, L. Joshi, *Biosens. Bioelectron.* **2007**, *23*, 428.
- [25] M. Berto, C. Diacci, R. D'Agata, M. Pinti, E. Bianchini, M. Di Lauro, S. Casalini, A. Cossarizza, M. Berggren, D. Simon, G. Spoto, F. Biscarini, C. A. Bortolotti, *Adv. Biosyst.* **2017**, *2*, 1700072.
- [26] W. Jung, J. Han, J. W. Choi, C. H. Ahn, *Microelectron. Eng.* **2015**, *132*, 46.
- [27] D. Karnaushenko, T. Kang, O. G. Schmidt, *Adv. Mater. Technol.* **2019**, *4*, 1800692.
- [28] D. Karnaushenko, T. Kang, V. K. Bandari, F. Zhu, O. G. Schmidt, *Adv. Mater.* **2019**, *32*, 1902994.
- [29] R. R. J. Richardson, J. A. Miller, W. M. Reichert, *Biomaterials* **1993**, *14*, 627.
- [30] B. Rubehn, T. Stieglitz, *Biomaterials* **2010**, *31*, 3449.
- [31] D. Karnaushenko, L. Baraban, D. Ye, I. Uguz, R. G. Mendes, M. H. Rummeli, J. A. G. M. De Visser, O. G. Schmidt, G. Cuniberti, D. Makarov, *Sci. Rep.* **2015**, *5*, 12878.
- [32] R. W. de Boer, A. van Oosterom, *Med. Biol. Eng. Comput.* **1978**, *16*, 1.
- [33] D. Karnaushenko, N. Münzenrieder, D. D. Karnaushenko, B. Koch, A. K. Meyer, S. Baunack, L. Petti, G. Tröster, D. Makarov, O. G. Schmidt, *Adv. Mater.* **2015**, *27*, 6797.
- [34] J. C. McDonald, D. C. Duffy, J. R. Anderson, D. T. Chiu, H. Wu, O. J. Schueller, G. M. Whitesides, *Electrophoresis* **2000**, *21*, 27.
- [35] M. A. Eddings, M. A. Johnson, B. K. Gale, *J. Micromech. Microeng.* **2008**, *18*, 067001.
- [36] L. P. Chia Gómez, P. Bollgruen, A. I. Egunov, D. Mager, F. Malloggi, J. G. Korvink, V. A. Luchnikov, *Lab Chip* **2013**, *13*, 3827.
- [37] S. C. Brooks, *Protoplasma* **1929**, *8*, 389.
- [38] G. N. Ling, G. Bohr, *Biophys. J.* **1970**, *10*, 519.
- [39] J. Stinnakre, *Trends Neurosci.* **1981**, *4*, 46.
- [40] R. Milo, R. Phillips, *Cell Biology by the Numbers*, Garland Science, New York **2016**.
- [41] J. B. Bates, Y. T. Chu, *Ann. Biomed. Eng.* **1992**, *20*, 349.
- [42] H. Ozbeck, S. L. Phillips, *Thermal Conductivity of Aqueous NaCl Solutions from 20 C to 330 C.*, University of California, Berkeley, CA **1979**.
- [43] H. R. Luckarift, P. Atanassov, G. R. Johnson, *Enzymatic Fuel Cells: From Fundamentals to Applications*, Wiley, Hoboken, NJ, **2014**.
- [44] N. Jaffrezic-Renault, S. V. Dzyadevych, *Sensors* **2008**, *8*, 2569.
- [45] M. B. Singh, R. Kant, *J. Electroanal. Chem.* **2013**, *704*, 197.
- [46] D. Austin, R. V. Kumar, *Ionics* **2005**, *11*, 262.
- [47] Y. Xu, X. Xie, Y. Duan, L. Wang, Z. Cheng, J. Cheng, *Biosens. Bioelectron.* **2016**, *77*, 824.
- [48] R. W. DeBlois, C. P. Bean, *Rev. Sci. Instrum.* **1970**, *41*, 909.
- [49] S. Gawad, K. Cheung, U. Seger, A. Bertsch, P. Renaud, *Lab Chip* **2004**, *4*, 241.
- [50] H. Morgan, T. Sun, D. Holmes, S. Gawad, N. G. Green, *J. Phys. D: Appl. Phys.* **2007**, *40*, 61.
- [51] W. Liang, Y. Zhao, L. Liu, Y. Wang, W. J. Li, G. Bin Lee, *Biophys. J.* **2017**, *113*, 1531.
- [52] H. H. Ussing, *Physiol. Rev.* **1949**, *29*, 127.
- [53] L. G. Filion, G. Graziani-Bowering, D. Matusevicius, M. S. Freedman, *Clin. Exp. Immunol.* **2003**, *131*, 324.
- [54] K. C. Dee, D. A. Puleo, R. Bizios, *An Introduction to Tissue-Biomaterial Interactions*, John Wiley & Sons, Inc., New York **2002**.
- [55] S. Noinville, F. Bruston, C. El Amri, D. Baron, P. Nicolas, *Biophys. J.* **2003**, *85*, 1196.
- [56] A. A. Patel, S. Yona, *Front. Immunol.* **2019**, *10*, 1.
- [57] K. Kranzer, A. Eckhardt, M. Aigner, G. Knoll, L. Deml, C. Speth, N. Lehn, M. Rehli, W. Schneider-Brachert, *Infect. Immun.* **2004**, *72*, 4416.

- [58] R. Landmann, H. P. Knopf, S. Link, S. Sansano, R. Schumann, W. Zimmerli, *Infect. Immun.* **1996**, *64*, 1762.
- [59] M. Daur, B. Obermaier, J. Herten, C. Haerle, K. Pohl, S. Rothenfusser, M. Schnurr, S. Endres, A. Eigler, *J. Immunol.* **2003**, *170*, 4069.
- [60] A. Schildberger, E. Rossmann, T. Eichhorn, K. Strassl, V. Weber, *Mediators Inflammation* **2013**, *2013*, 697972.
- [61] L. A. Lyakh, G. K. Koski, W. Telford, R. E. Gress, P. A. Cohen, N. R. Rice, *J. Immunol.* **2000**, *165*, 3647.
- [62] C. E. Henriksson, O. Klingenberg, R. Øvstebø, G. B. Jøø, Å. B. Westvik, P. Kierulf, *Thromb. Haemostasis* **2005**, *94*, 1236.
- [63] B. Liu, R. Sun, H. Luo, X. Liu, M. Jiang, C. Yuan, L. Yang, J. Hu, *Immunobiology* **2017**, *222*, 198.
- [64] C. H. Jang, J. H. Choi, M. S. Byun, D. M. Jue, *Rheumatology* **2006**, *45*, 703.
- [65] S. Iwamoto, S. Iwai, K. Tsujiyama, C. Kurahashi, K. Takeshita, M. Naoe, A. Masunaga, Y. Ogawa, K. Oguchi, A. Miyazaki, *J. Immunol.* **2007**, *179*, 1449.
- [66] A. Prasse, M. Germann, D. V. Pechkovsky, A. Markert, T. Verres, M. Stahl, I. Melchers, W. Luttmann, J. Müller-Quernheim, G. Zissel, *J. Allergy Clin. Immunol.* **2007**, *119*, 464.
- [67] D. D. Karnaushenko, D. Karnaushenko, D. Makarov, O. G. Schmidt, *NPG Asia Mater* **2015**, *7*, e188.